

JotlasNet: Joint Tensor Low-Rank and Attention-based Sparse Unrolling Network for Accelerating Dynamic MRI

Yinghao Zhang^a, Haiyan Gui^b, Ningdi Yang^b and Yue Hu^{a,*}

^aSchool of Electronics and Information Engineering, Harbin Institute of Technology, Harbin, China

^bThe Fourth Hospital of Harbin, Harbin, China

ARTICLE INFO

Keywords:

deep unrolling network
tensor low rank
attention-based sparse
dynamic MRI
composite splitting algorithm

ABSTRACT

Joint low-rank and sparse unrolling networks have shown superior performance in dynamic MRI reconstruction. However, existing works mainly utilized matrix low-rank priors, neglecting the tensor characteristics of dynamic MRI images, and only a global threshold is applied for the sparse constraint to the multi-channel data, limiting the flexibility of the network. Additionally, most of them have inherently complex network structure, with intricate interactions among variables. In this paper, we propose a novel deep unrolling network, JotlasNet, for dynamic MRI reconstruction by jointly utilizing tensor low-rank and attention-based sparse priors. Specifically, we utilize tensor low-rank prior to exploit the structural correlations in high-dimensional data. Convolutional neural networks are used to adaptively learn the low-rank and sparse transform domains. A novel attention-based soft thresholding operator is proposed to assign a unique learnable threshold to each channel of the data in the CNN-learned sparse domain. The network is unrolled from the elaborately designed composite splitting algorithm and thus features a simple yet efficient parallel structure. Extensive experiments on two datasets (OCMR, CMRxRecon) demonstrate the superior performance of JotlasNet in dynamic MRI reconstruction.

1. Introduction

Accelerating magnetic resonance imaging (MRI) has become a highly crucial research direction in the MRI research community [1]. For dynamic MRI that captures temporal changes, a larger amount of data needs to be collected. The demand for reducing imaging time is more urgent in this context, and the required acceleration factor is also higher. Currently, acquiring k-space data below the Nyquist sampling rate is the primary approach for accelerating MRI [2, 3]. However, this undersampling strategy inevitably leads to image aliasing artifacts, creating a trade-off between acceleration and image quality. Therefore, it is paramount to design reconstruction algorithms that can enhance image quality at a fixed acceleration factor or, in other words, tolerate higher acceleration factors while meeting clinical requirements for image quality.

In recent decades, iterative optimization algorithms have emerged as promising tools for accelerating MRI [2]. Specifically, explicit prior about MRI images is incorporated as a constraint term, combined with the fidelity term of k-space data, to construct an optimization reconstruction model. Iterative algorithms like ADMM (Alternating Direction Method of Multipliers) [4, 5] and ISTA (Iterative Shrinkage-Thresholding Algorithm) [6] are commonly employed to tackle these optimization problems. Sparse priors, a fundamental aspect of compressive sensing, have been widely employed in MRI reconstruction [3, 7–9]. Additionally, methods leveraging matrix/tensor low-rank priors [10, 11] have been proposed. Moreover, hybrid approaches combining

low-rank and sparse priors have demonstrated superior performance compared to single-prior methods. These hybrids typically fall into two categories: one involves a low-rank plus sparse scheme [12], where dynamic MRI images are partitioned into slowly varying low-rank backgrounds and rapidly changing sparse components; the other is a joint low-rank and sparse formulation [13], simultaneously applying low-rank and sparse constraints to the target image to fully exploit data prior features. We focus our discussion on the latter category in this paper. Despite the notable progress of these optimization methods, they face several common challenges: **a.** convergence often requires a considerable number of iterations, resulting in lengthy reconstruction times; **b.** manual tuning of hyperparameters based on small dataset reconstructions is common, lacking robustness and time-consuming.

Deep unrolling networks (DUNs) [14] effectively address the aforementioned issues by unfolding fixed-number iterations of the optimization algorithm into a deep learning network. This transformation turns the hyperparameters of the original iterative algorithm into learnable parameters within the network. Subsequently, these parameters can be trained in an end-to-end supervised manner on large datasets, eliminating the need for manual tuning. Furthermore, DUNs can leverage neural networks such as CNN (convolutional neural network) to learn a suitable transform domain, enhancing reconstruction accuracy by more efficiently utilizing the explicit priors. After sufficient training, DUNs can achieve rapid reconstruction at test time (within seconds) [15, 16]. Additionally, due to their ability to leverage explicit data priors and their unfolded feature, DUNs exhibit strong interpretability—an attribute not typically found in traditional deep learning networks. To date, DUNs have proven to be the most outstanding reconstruction method

*Corresponding author: e-mail: huyue@hit.edu.cn

ORCID(s): 0000-0001-8501-6180 (Y. Zhang); 0000-0002-4648-611X (Y.

Hu)

in the field of MRI reconstruction [1]. However, current DUNs for accelerating dynamic MRI face some challenges. **a.** Tensor low-rank priors have demonstrated the ability to efficiently exploit high-dimensional structural similarities in optimization-based methods, thereby achieving superior performance. However, in joint low-rank and sparse DUNs, the low-rank priors are typically derived from the Casorati matrix, neglecting the tensor characteristics of dynamic MRI images. **b.** The two CNNs (see LR or S layer in Fig.1) that learn the transform domain for efficiently utilizing explicit priors, are usually constrained to be inverse, limiting the flexibility of the network. **c.** In the CNN-learned sparse transform domain, data is represented as multi-channel features. However, current networks [15, 17] typically apply the same thresholding operation to all channels using traditional soft thresholding (ST) [18] operators. **d.** Current iterative optimization algorithms for joint low-rank and sparse unrolling networks [15] are highly complex and involve numerous temporary variables and intricate interactions. This complexity renders the design of composite-prior DUNs difficult and cumbersome, while also hindering efficient backpropagation to some extent, consequently leading to suboptimal reconstruction results.

The tensor nuclear norm [19] based on tensor singular value decomposition (t-SVD) [20] effectively leverages the low-rank characteristics of tensors and has demonstrated excellent performance across various applications [21, 22]. Compared to traditional tensor CP and Tucker decompositions [23], t-SVD offers a rigorously defined tensor nuclear norm, which can be theoretically proven to be the convex envelope of the tensor rank. The computation of t-SVD can be achieved by performing SVD on multiple matrices along a specific dimension, eliminating the need for the iterative optimization process required by CP decomposition, thereby significantly reducing computational complexity. The recent development of transformd t-SVD [21] has provided theoretical support for the low-rank prior learned in the CNN transform domain. This advancement allows CNNs to effectively extract low-rank information from data, leveraging the low-rank prior in a theoretically sound manner. Additionally, the composite splitting algorithm [24] for models with joint dual priors, directly utilizes the ISTA algorithm for solving, resulting in a simple algorithmic structure. Moreover, it has been demonstrated to achieve faster convergence speed and better reconstruction performance compared to complex ADMM-based algorithms [24].

Inspired by these findings, in this paper, we proposed a novel JotlasNet: joint tensor low-rank and attention-based sparse unrolling network for accelerating dynamic MRI, with the following contributions for the aforementioned challenges.

- Propose a novel network incorporating tensor low-rank and attention-based sparse priors for dynamic MRI reconstruction. The tensor low-rank prior is derived from t-SVD, effectively exploiting the structural correlations within high-dimensional data. The CNNs adaptively learn the low-rank and sparse transforms

without constraints, allowing the JotlasNet to simultaneously exploit explicit priors and implicit CNN-extracted features.

- Introduce an Attention-based Soft Thresholding operator (AST), assigning a learnable threshold to each channel of the data in the CNN-learned sparse domain. This enhances the flexibility of the tensor sparse constraint, thereby improving the reconstruction quality.
- Develop a simple yet efficient structure for the joint low-rank and sparse unrolling network based on the composite splitting algorithm.
- Extensive experiments on two publicly available datasets (OCMR, CMRxRecon) demonstrate the superior performance of the proposed JotlasNet in dynamic MRI reconstruction.

Although our preliminary work was presented at ICIP 2023 [25], this paper represents a significant extension. Unlike our prior work, which solely relied on sparse priors, this paper introduces a network combining both low-rank and sparse priors. Furthermore, it explores the high-dimensional structural correlations in the data using tensor low-rank prior. Additionally, we have carefully designed the network structure for joint priors and enriched both experimental and theoretical aspects.

2. Related Works

2.1. General Reconstruction Model of Dynamic MRI

The acquisition of dynamic MRI can be formulated as,

$$\mathbf{b} = \mathbf{A}(\mathcal{X}) + \mathbf{n}, \quad (1)$$

where $\mathbf{b} \in \mathbb{C}^M$ is the acquired k-space data, $\mathcal{X} \in \mathbb{C}^{H \times W \times T}$ is the distortion-free dynamic MRI image with H , W , and T representing the spatial dimensions and temporal frames, respectively, $\mathbf{A} : \mathbb{C}^{H \times W \times T} \rightarrow \mathbb{C}^M$ is the acquisition operator, and $\mathbf{n} \in \mathbb{C}^M$ is the noise. From the above equation, it can be observed that reconstructing the clean image \mathcal{X} from the acquired undersampled k-space data \mathbf{b} is a typical ill-posed linear inverse problem. Specifically, based on the physical principles of MRI, operator \mathbf{A} can be expressed in a more detailed manner,

$$\mathbf{A} = \mathbf{F}_u \circ \mathbf{S} = \mathbf{M} \circ \mathbf{F} \circ \mathbf{S}, \quad (2)$$

where \mathbf{F}_u is the undersampling operator, $\mathbf{S} : \mathbb{C}^{H \times W \times T} \rightarrow \mathbb{C}^{C \times H \times W \times T}$ denotes the coil sensitive maps for multi-coil MRI with C coils, and the symbol \circ denotes the composite operation. When the sampling points are in the Cartesian grid, $\mathbf{F}_u = \mathbf{M} \circ \mathbf{F}$ holds with \mathbf{F} being the unitary Fourier transform, and \mathbf{M} denoting the sampling mask. As for single-coil cases, \mathbf{S} can be omitted.

Based on (1), the reconstruction model of dynamic MRI can be formulated as,

$$\hat{\mathcal{X}} = \arg \min_{\mathcal{X}} \frac{1}{2} \|\mathbf{A}(\mathcal{X}) - \mathbf{b}\|_2^2 + \lambda \Phi(\mathcal{X}), \quad (3)$$

where the first term with l_2 norm is the data fidelity term, the second term with $\Phi : \mathbb{C}^{H \times W \times T} \rightarrow \mathbb{R}_+$ is the regularization term that encodes the prior information of MRI images, and λ is the balance parameter.

2.2. Unrolling Networks using Single Prior

An unrolling network [14, 26, 27] generally involves three factors: a prior-driven reconstruction model, an iterative solving algorithm, and unfolding. Actually, the first two factors can precisely constitute a complete optimization-based reconstruction method.

In recent years, various unrolling reconstruction networks based on a single prior have emerged and become mainstream [1]. DCCNN [16], MoDL [28], and E2EVarNet [29] are representative examples that using CNNs to learn the implicit image prior. HUMUS-Net [30] took the vision Transformer to substitute CNN. CineVN [31] employed a spatiotemporal E2EVarNet combined with conjugate gradient descent for optimized data consistency and improved image quality for dynamic MRI. However, the implicit nature leads to a lack of interpretability. ISTA-Net [17] and FISTA-Net [32] exploited the learned sparse prior and adopted the ST operator [18] to enforce the sparsity constraint in a CNN-learned multi-channel sparse domain. However, the ST operator applied the same threshold to all channels and the two CNNs that learn the sparse transforms are constrained to be inverse, limiting the flexibility of the sparse constraint. Moreover, T2LR-Net [21, 33] utilized the tensor low-rank prior and the tensor nuclear norm [20] to exploit the structural correlations in high-dimensional data, in which CNNs were also used to adaptively learn the low-rank transform domain.

As for the underlying iterative solving algorithms that we termed as the structure of the DUNs, algorithms like ADMM [4], ISTA [6], and others are widely used. However, although ADMM is an effective algorithm for a lot of optimization problems, it usually requires the conjugate gradient (CG) method to solve the subproblems, especially for the MRI reconstruction cases with non-Cartesian sampling and multi-coil data. Inserting CG in DUNs will increase the complexity of the network and make the training process more difficult [28]. ISTA does not require CG iterations; it can be iteratively solved through a gradient descent step and a projection step. Another widely used approach is to directly simplify the gradient descent step in ISTA through the use of the Data Consistency (DC) layer [16, 29]. The ISTA algorithm for solving (3) can be formulated as,

$$\begin{cases} \bar{\mathcal{X}} = \mathcal{X}^n - \mu \nabla_{\mathcal{X}} \left[\frac{1}{2} \|\mathbf{A}(\mathcal{X}) - \mathbf{b}\|_2^2 \right] = \mathcal{X}^n - \mu \mathbf{A}^H [\mathbf{A}(\mathcal{X}^n) - \mathbf{b}] \\ \mathcal{X}^{(k+1)} = \arg \min_{\mathcal{X}} \frac{1}{2\mu} \|\mathcal{X} - \bar{\mathcal{X}}\|_2^2 + \lambda \Phi(\mathcal{X}) = \text{prox}_{\mu\lambda\Phi}(\bar{\mathcal{X}}), \end{cases} \quad (4)$$

where the operator $\text{prox}_{\mu\lambda\Phi}(\cdot)$ is the projection onto the set defined by the regularization Φ with the threshold $\mu\lambda$, with μ being the step size.

2.3. Unrolling Networks using Composite Priors

Composite priors-driven DUNs in dynamic MRI reconstruction mainly lie in the intersection of the low-rank and sparse priors. LplusS-Net [34] and SLR-Net [15] represent two different types, where the former follows a low-rank plus sparse scheme, while the latter adopts a joint low-rank and sparse formulation which is the focus of this paper. Additionally, SOUL-Net [35] utilizes similar structures to SLR-Net but is applied in CT reconstruction. JSLR-Net [36] also follows the joint low-rank and sparse scheme, but it is unfolded by the HQS algorithm, which may need conjugate gradient (CG) iterations to solve the subproblems. However, CG iterations will increase the complexity of the network and make the training process more difficult [28].

In SLR-Net, the low-rank prior is leveraged through the Casorati matrix. The Casorati matrix is obtained by unfolding the dynamic MRI tensor \mathcal{X} along the temporal dimension, resulting in an $HW \times T$ matrix. The nuclear norm of this matrix is then utilized to explore the correlation of temporal evolution curves. However, this approach neglects spatial correlations, and the process of unfolding a high-dimensional tensor into a matrix inevitably loses the high-dimensional structural features of the data. Therefore, we believe a superior approach would be to employ tensor low-rank priors to construct the network.

Furthermore, the joint low-rank and sparse model can be formulated as,

$$\min_{\mathcal{X}} \frac{1}{2} \|\mathbf{A}(\mathcal{X}) - \mathbf{b}\|_2^2 + \lambda_1 \mathbf{R}(\mathcal{X}) + \lambda_2 \mathbf{S}(\mathcal{X}), \quad (5)$$

where $\mathbf{R}(\mathcal{X})$ and $\mathbf{S}(\mathcal{X})$ denote the LR and sparse priors, respectively. λ_1 and λ_2 are the balancing parameters. SLR-Net has developed an algorithm that embeds ISTA within ADMM. Specifically, using ADMM and introducing auxiliary variables \mathcal{T} , the optimization problem (5) can be reformulated as,

$$\begin{cases} \min_{\mathcal{X}} \frac{1}{2} \|\mathbf{A}(\mathcal{X}) - \mathbf{b}\|_2^2 + \frac{\rho}{2} \|\mathcal{X} - \mathcal{T}\|_F^2 + \lambda_2 \mathbf{S}(\mathcal{X}) \\ \min_{\mathcal{T}} \frac{\rho}{2} \|\mathcal{X} - \mathcal{T}\|_F^2 + \lambda_1 \mathbf{R}(\mathcal{T}) \\ \mathcal{L} = \mathcal{L} + \eta(\mathcal{X} - \mathcal{T}), \end{cases} \quad (6)$$

where \mathcal{L} is the Lagrangian multiplier. ISTA is then embedded to solve the \mathcal{X} subproblem, resulting in,

$$\begin{cases} \begin{cases} \mathcal{Z} = \mathcal{X} - \mu \nabla_{\mathcal{X}} \left[\frac{1}{2} \|\mathbf{A}(\mathcal{X}) - \mathbf{b}\|_2^2 + \frac{\rho}{2} \|\mathcal{X} - \mathcal{T}\|_F^2 \right] \\ \min_{\mathcal{X}} \frac{1}{2\mu} \|\mathcal{X} - \mathcal{Z}\|_2^2 + \lambda_2 \mathbf{S}(\mathcal{X}) \end{cases} \\ \min_{\mathcal{T}} \frac{\rho}{2} \|\mathcal{X} - \mathcal{T}\|_F^2 + \lambda_1 \mathbf{R}(\mathcal{T}) \\ \mathcal{L} = \mathcal{L} + \eta(\mathcal{X} - \mathcal{T}). \end{cases} \quad (7)$$

Note that we have omitted the indexing notation for iterations for the sake of brevity. From the above equation, it is evident that the interactions among the three temporary variables, \mathcal{Z} , \mathcal{T} , and \mathcal{L} , are relatively complex. This complexity renders the design of composite-prior DUNs difficult and cumbersome, while also hindering efficient backpropagation to some extent, consequently leading to suboptimal reconstruction results. We believe that a more simple iterative solving

algorithm can also lead to a more efficient unrolling network structure and, consequently, achieving better reconstruction results and simplifying network design.

3. Method

3.1. Composite Splitting Algorithm for Joint Low-Rank and Sparse Model

The dynamic MRI image is a 3-way tensor and exhibits high-dimensional data structures and correlations. Therefore, we construct the low-rank and sparse regularizations from the perspective of tensor.

Specifically, the tensor low-rank regularization is constructed based on the transformed tensor nuclear norm (TTNN) [21] under the framework of t-SVD [20], which is defined

$$\mathbf{R}(\mathcal{X}) = \sum_{i=1}^T \|\mathbf{T}(\mathcal{X})^{(i)}\|_* \quad (8)$$

In the above equation, the operator $\|\cdot\|_*$ denotes the nuclear norm of a matrix, which is the sum of its singular values, and \mathbf{T} is a CNN-learned transformation that maps the input tensor to a low-rank domain. The subscript (i) denotes the i -th frontal slice of the tensor, i.e., for a tensor $\mathcal{Y} = \mathbf{T}(\mathcal{X})$, $\mathcal{Y}^{(i)} = \mathcal{Y}(:, :, i)$, $i = 1, 2, \dots, T$ holds.

The TTNN can be interpreted as the sum of the nuclear norms of the frontal slices in the transformed domain. The transformation \mathbf{T} applied to the entire tensor allows for the extraction of high-dimensional structural information. Consequently, within the transformed domain, any frontal slice may encompass all the information from the original image domain. While we aim to provide a comprehensive interpretation of TTNN, it is essential to note that TTNN possesses a complete and rigorous mathematical definition and derivation (see [21]).

The tensor sparse regularization is constructed based on the tensor l_1 norm in the CNN-learned domain, which is defined as,

$$\mathbf{S}(\mathcal{X}) = \|\mathbf{D}(\mathcal{X})\|_1, \quad (9)$$

where \mathbf{D} is a CNN-learned transformation that maps the input tensor to a sparse domain. The tensor l_1 norm is the sum of the absolute values of all elements in the tensor.

To efficiently solve the joint low-rank and sparse model (5), the optimization problem (5) can be decomposed into the following subproblems using the composite splitting algorithm [24, 37],

$$\bar{\mathcal{X}} = \mathcal{X}^n - \mu \mathbf{A}^H [\mathbf{A}(\mathcal{X}^n) - \mathbf{b}], \quad (10)$$

$$\mathcal{Y}_1 = \arg \min_{\mathcal{X}} \frac{\omega_1}{2\mu} \|\mathcal{X} - \bar{\mathcal{X}}\|_F^2 + \lambda_1 \mathbf{R}(\mathcal{X}), \quad (11)$$

$$\mathcal{Y}_2 = \arg \min_{\mathcal{X}} \frac{\omega_2}{2\mu} \|\mathcal{X} - \bar{\mathcal{X}}\|_F^2 + \lambda_2 \mathbf{S}(\mathcal{X}), \quad (12)$$

$$\mathcal{X}^{n+1} = \omega_1 \mathcal{Y}_1 + \omega_2 \mathcal{Y}_2, \quad (13)$$

where the first step is the gradient descent, the second and the third steps are the projection steps, and ω_1 and ω_2 with $\omega_1 + \omega_2 = 1$ are the balancing parameters.

From (8) and the corresponding transformed tensor singular value thresholding algorithm [21], the \mathcal{Y}_1 subproblem can be solved as,

$$\mathcal{Y}_1 = \mathbf{T}^H \circ \text{SVT}_{\frac{\mu\lambda_1}{\omega_1}} \circ \mathbf{T}(\bar{\mathcal{X}}), \quad (14)$$

where $\text{SVT}_{\tau}(\cdot)$ is the singular value thresholding operator with threshold τ for each frontal slice of the tensor and \mathbf{T}^H is the adjoint transformation of \mathbf{T} . We further employ a widely used trick [15] to allocate a distinct threshold to each frontal slice individually (more details in Section 3.2.1).

The \mathcal{Y}_2 subproblem can be solved by the soft thresholding operator [18] in the transformed domain, i.e.,

$$\mathcal{Y}_2 = \mathbf{D}^H \circ \text{ST}_{\frac{\mu\lambda_2}{\omega_2}} \circ \mathbf{D}(\bar{\mathcal{X}}), \quad (15)$$

where $\text{ST}_{\tau}(\cdot)$ is the soft thresholding operator with threshold τ for each element of the tensor. It is worth noting that the ST operator only uses a single threshold for all elements in the tensor, which may limit the flexibility of the sparse constraint. We propose a novel attention-based soft thresholding operator in Section 3.2.2 to address this issue.

From the above algorithm, it can be observed that our designed algorithm possesses an efficient yet simple structure. Intermediate variables $\bar{\mathcal{X}}$ and \mathcal{Y} interact only within the current iteration, avoiding intricate relationships between iterations, unlike the algorithm (7) in SLR-Net [15]. Moreover, our algorithm can be considered a reasonable extension of ISTA, exhibiting a similar alternation of two ISTA ($\mathbf{R}(\mathcal{X})$ and $\mathbf{S}(\mathcal{X})$ -constrained ISTAs) with the addition of a linear combination of two proximal mappings in the last iteration step (13). Therefore, building upon the widespread recognition and application of ISTA in the DUN community, our algorithm also inherits the advantages of ISTA for DUNs.

Additionally, similar to ISTA's ability to incorporate the Nesterov acceleration step for improved convergence speed, and as demonstrated by FISTA-Net [32], adding the acceleration step can enhance reconstruction effectiveness. Thus, inspired by these findings, we also integrate Nesterov acceleration steps into our algorithm. In summary, our algorithm is depicted in Alg.1.

3.2. JotlasNet

Unfolding Alg.1 into a DUN allows for transformations and hyperparameters therein becoming neural networks and learnable parameters. Therefore, we can also further enhance the flexibility by assigning a unique set of parameters to each iteration. Finally, we propose the JotlasNet as shown

Algorithm 1: Composite Splitting Algorithm for Joint Low-Rank and Sparse Model

Require : $\{\mathbf{T}, \mathbf{T}^H, \mathbf{D}, \mathbf{D}^H, \mu, \lambda_1, \lambda_2, \omega_1, \omega_2\}$
Initialize: $\mathcal{X}^0 = \mathbf{A}^H \mathbf{b}$, $t^0 = 1$
for $n = 1, \dots$, *until convergence* **do**

$$\bar{\mathcal{X}} = \mathcal{X}^n - \mu \mathbf{A}^H [\mathbf{A}(\mathcal{X}^n) - \mathbf{b}];$$

$$\mathcal{Y}_1 = \mathbf{T}^H \circ \text{SVT}_{\frac{\mu\lambda_1}{\omega_1}} \circ \mathbf{T}(\bar{\mathcal{X}});$$

$$\mathcal{Y}_2 = \mathbf{D}^H \circ \text{ST}_{\frac{\mu\lambda_2}{\omega_2}} \circ \mathbf{D}(\bar{\mathcal{X}});$$

$$\mathcal{Z}^n = \omega_1 \mathcal{Y}_1 + \omega_2 \mathcal{Y}_2;$$

Acceleration Step:

$$t^{n+1} = \frac{1 + \sqrt{1 + 4(t^n)^2}}{2};$$

$$\mathcal{X}^{n+1} = \mathcal{Z}^n + \frac{t^n - 1}{t^{n+1}} (\mathcal{Z}^n - \mathcal{Z}^{n-1})$$

end

in Fig.1, which is unfolded from the following algorithm.

$$\begin{cases} \bar{\mathcal{X}} &= \mathcal{X}^n - \mu^n \mathbf{A}^H [\mathbf{A}(\mathcal{X}^n) - \mathbf{b}] \\ \mathcal{Y}_1 &= \tilde{\mathbf{T}}^n \circ \text{SVT}_{t^n/\omega_1} \circ \mathbf{T}^n(\bar{\mathcal{X}}) \\ \mathcal{Y}_2 &= \tilde{\mathbf{D}}^n \circ \text{AST}_{\vec{t}^n/\omega_2} \circ \mathbf{D}^n(\bar{\mathcal{X}}) \\ \mathcal{Z}^n &= \omega_1^n \mathcal{Y}_1 + \omega_2^n \mathcal{Y}_2 \\ \mathcal{X}^{n+1} &= \mathcal{Z}^n + t^n (\mathcal{Z}^n - \mathcal{Z}^{n-1}) \end{cases}, \quad (16)$$

where we replace $\mu\lambda_1$ and $\frac{t^n-1}{t^{n+1}}$ with a single learnable parameter th and t , respectively. The ST operator with a single threshold $\mu\lambda_2$ is replaced by the proposed AST operator with a vector of thresholds \vec{t} for each channel of the input data. The red-marked symbols in Fig.1 are learnable and the superscript n denotes they are unique for each iteration.

The JotlasNet consists of five layers, the Gradient Descent (GD), Low-Rank (LR), Sparse (S), combination and Acceleration (ACC) layers, corresponding to the five steps of (16), respectively. Except for the LR and S layers, the remaining layers are not incorporated with neural networks, such as CNN. Instead, they are computed in the deep learning framework according to the iterative algorithm's formulas, with only the parameters becoming trainable. It is worth noting that $\mu > 0$, $\omega_1 + \omega_2 = 1$, and $t \in [0, 1]$. We can apply ReLU, softmax, and sigmoid functions to reasonably constrain the parameters accordingly. The LR and S layers are described in detail as follows.

3.2.1. The LR Layer

This layer corresponds to the \mathcal{Y}_1 step in Eq.(16). We utilize two independent CNNs to learn the transformations \mathbf{T}^H and \mathbf{T} in Alg.1, denoted as $\tilde{\mathbf{T}}$ and \mathbf{T} , respectively. These two CNNs share the same structure, consisting of three 3D convolutional layers with kernel sizes of $3 \times 3 \times 3$ and the stride of 1. The output channels for the three convolutional layers are Nc , Nc , and 2, respectively. The reason for having 2 channels in the last convolutional layer is that we

split the MRI complex data into real and imaginary parts. Two ReLU activation functions are interspersed between the three convolutional layers, with the last convolutional layer not being activated to ensure that negative values are not truncated in the output. In the CNN transformation domain, we synthesize the dual-channel real data into complex data, which we denote as \mathcal{F}_1 . The learned SVT operator in the middle is applied to each frontal slice of \mathcal{F}_1 . For the i -th frontal slice with its singular value decomposition (SVD) as $\mathcal{F}_1^{(i)} = \mathbf{U}\mathbf{\Sigma}\mathbf{V}^H$, the learned SVT operates as follows.

$$\text{SVT}_{th/\omega_1}(\mathcal{F}_1^{(i)}) = \mathbf{U} \cdot \text{ReLU} \left(\mathbf{\Sigma} - \frac{\text{sigmoid}(th) \cdot \sigma_{max}}{\omega_1} \right) \cdot \mathbf{V}^H \quad (17)$$

where we omit the superscript n for brevity, σ_{max} is the maximum singular value of $\mathcal{F}_1^{(i)}$, and $\text{sigmoid}(\cdot)$ is the sigmoid function.

It is worth noting that during the unrolling process, we relax the constraint in Alg.1 that \mathbf{T}^H and \mathbf{T} must be adjoint, allowing the two CNNs to learn freely from the data. This approach enables us to simultaneously utilize explicit low-rank priors and implicit image prior information extracted by CNNs, thereby enhancing the reconstruction performance [21]. Specifically, if the threshold th is learned to be close to zero or a very small value during training, the LR layer will effectively become a pure CNN layer, capable of learning additional prior information beyond low-rank constraints that may be required for reconstruction.

3.2.2. The S Layer

Similar to the LR layer, this layer corresponds to the \mathcal{Y}_2 step in Eq.(16). Similarly, we use two independent CNNs to learn the transformations \mathbf{D}^H and \mathbf{D} in Alg.1, denoted as $\tilde{\mathbf{D}}$ and \mathbf{D} , respectively. Unlike the LR layer, the output channels of the third convolutional layer used to learn $\tilde{\mathbf{D}}$ are set to Nc to increase data dimensionality and redundancy, thereby extracting richer sparse prior information. This is mainly due to the sparse constraint not requiring SVD, resulting in lower computational complexity. Additionally, in the CNN transform domain, we do not synthesize dual-channel real data into complex data; instead, we directly impose sparse constraints on each channel.

Current DUNs implement sparse constraints using an ST operator, where only one threshold is used to constrain data across all channels. We believe that this approach may limit the expressive power of sparse constraints, as data in different channels may exhibit different sparsity patterns. Therefore, inspired by [38], we propose a novel Attention-based Soft Thresholding operator (AST), assigning a learnable threshold to each channel of the data in the CNN-learned sparse domain. The diagram of AST is shown in Fig. 1. Specifically, for an input data \mathcal{F}_2 of size $Nc \times H \times W \times T$, AST first takes the absolute value and performs global average pooling (GAP) to obtain a vector \mathbf{f} of size $Nc \times 1$. Then, two fully connected layers separated by ReLU activation and later the sigmoid function are utilized

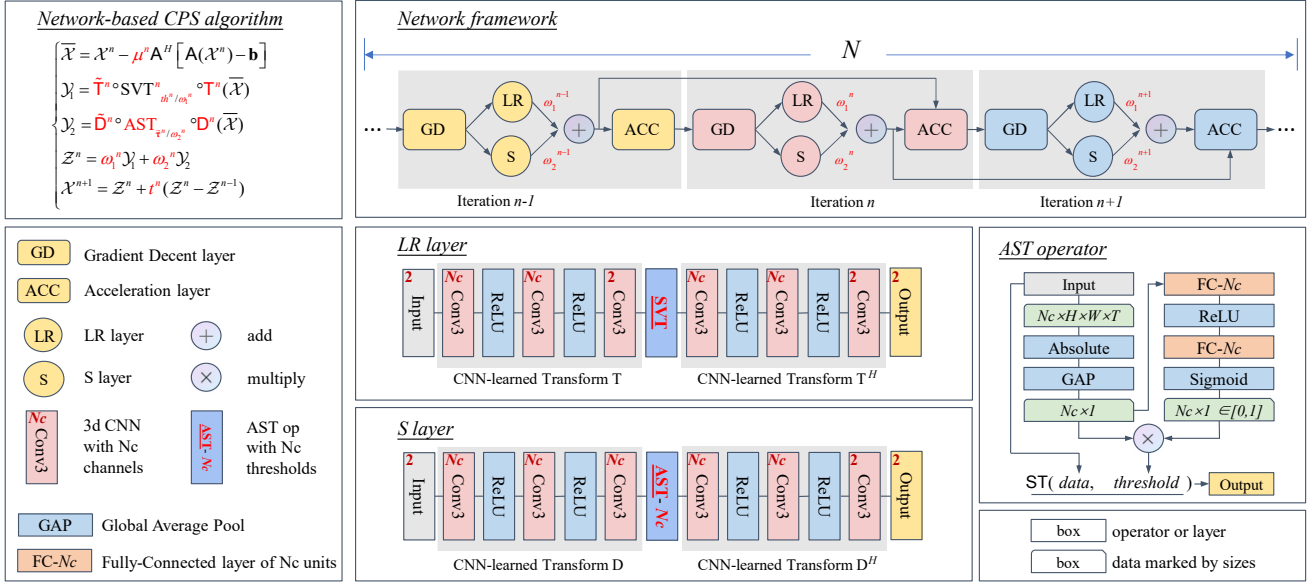


Figure 1: The proposed JotlasNet. The network is unfolded from (16). The red-marked symbols are learnable parameters. Five layers are included: Gradient Decent (GD), Low-Rank (LR), Sparse (S), combination, and Acceleration (ACC) layers. The LR and S layers are detailed in the text.

to obtain a self-attention weight vector $\vec{\mathbf{w}}$. Element-wise multiplication of $\vec{\mathbf{w}}$ and $\vec{\mathbf{f}}$ yields an adaptive sparse threshold vector $\vec{\tau} = [\tau_1, \tau_2, \dots, \tau_{N_c}]^T$. Finally, the ST operator with the threshold τ_i is applied to the i -th channel of the data $\mathcal{F}_2^{[i]}$ as follows.

$$\text{ST}_{\tau_i/\omega_2}(\mathcal{F}_2^{[i]}) = \frac{\mathcal{F}_2^{[i]}}{|\mathcal{F}_2^{[i]}|} \cdot \text{ReLU} \left(|\mathcal{F}_2^{[i]}| - \frac{\tau_i}{\omega_2} \right) \quad (18)$$

where $|\mathcal{F}_2^{[i]}|$ denotes the absolute value of $\mathcal{F}_2^{[i]}$ and $\frac{\tau_i}{|\mathcal{F}_2^{[i]}|}$ is the element-wise divide operation, i.e., the sign function of $\mathcal{F}_2^{[i]}$.

3.2.3. Loss Function

We utilize the mean squared error (MSE) as the loss function, i.e.,

$$\text{Loss} = \sum_{(\mathcal{X}_{GT}, \mathbf{b}) \in \Omega} \|\mathcal{X}_{GT} - f_{net}(\mathbf{b}|\theta)\|_F^2. \quad (19)$$

where Ω is the training set, \mathcal{X}_{GT} is the ground truth, $f_{net}(\mathbf{b}|\theta)$ is the output of the network with parameters $\theta = \{\mathbf{T}^n, \bar{\mathbf{T}}^n, \mathbf{D}^n, \bar{\mathbf{D}}^n, \mu^n, t^n, \tau^n, \omega_1^n, \omega_2^n, FC^n | n = 1 \dots N\}$, and FC denotes the two fully connected layers in the AST operator.

3.2.4. Implementation Details

Considering the trade-off between computational burden and reconstruction accuracy, we set the number of iterations (N) for JotlasNet to 15. The number of channels for convolutional layers or hidden units for fully connected layers (N_c) is set to 16, resulting in a total of about 708k parameters. We train the network using the Adam optimizer [39] with

parameters $\beta_1 = 0.9$, $\beta_2 = 0.999$, $\epsilon = 10^{-8}$, and an initial learning rate of 0.001, decayed by a factor of 0.95 [40]. The model is implemented using the TensorFlow framework [41] with a batch size of 1.

3.2.5. Computational Complexity

Suppose that the input of JotlasNet \mathcal{X} has the size of $H \times W \times T$ with $H > W$, and the number of coils is denoted as C . The GD layer only consists of linear operations and repeated fast Fourier transforms on H and W spatial dimensions across temporal dimension T and coil channel C , resulting in a complexity of $\mathcal{O}(HW \log(HW)TC)$. For the S layer, the total complexity of the two CNNs (the transform \mathbf{D} and its transpose) is $HWT \times 3^3 \times 16 \times (16 + 16 + 2) \times 2$, i.e., $\mathcal{O}(HWT)$. Here, we directly use the kernel size and the number of channels from the implementation details to simplify the calculation. The cost of the AST operator is dominated by linear operations, leading to a complexity of $\mathcal{O}(HWT)$. Note that the calculation of the attention maps depends on the number of channels, which is negligible compared to the linear operations. For the LR layer, the two CNNs have the same complexity as the S layer, resulting in $\mathcal{O}(HWT)$. The SVT operator is dominated by the tensor SVD, whose complexity is $\mathcal{O}(HW^2T)$. The ACC layer only involves linear operations, resulting in a complexity of $\mathcal{O}(HWT)$. Therefore, for N iterations, the total complexity of JotlasNet is $\mathcal{O}(NHWT(\log(HW)C + W))$.

4. Experiments and Results

4.1. Datasets and Experimental Setup

We conducted experiments on two publicly available cardiac cine MRI datasets, OCMR and CMRxRecon. The

Table 1
Datasets and Experimental Setup

dataset	coil	sampling	section
OCMR	single-coil	radial-16,30 ; VDS-8,10	4.2, 4.4
	multi-coil	VISTA-8,12,24	4.3
CMRxRecon	multi-coil	equispaced-4,8,10	4.3

specific datasets and experimental configurations are listed in Tab.1.

4.1.1. OCMR Dataset

This dataset [42] consists of 204 fully sampled cardiac cine MRI raw data, which were acquired from 74 subjects collected on three Siemens MAGNETOM scanners: Prisma (3T), Avanto (1.5T), and Sola (1.5T). Both the short-axis and long-axis views are included. For our experiments, we allocated 124 data for training, 40 for validation, and 40 for testing. For the training set, considering the limited data quantity, we applied appropriate data augmentation techniques. We cropped the data to a size of $128 \times 128 \times 16$ based on the dimensions of all data in the training set, with strides of 32, 32, and 8 in the spatial (height, width) and temporal directions, respectively. Finally, a total of 1848 fully sampled training samples were obtained.

In our experiments on this dataset, both single-coil and multi-coil scenarios were considered. For the single-coil experiments, we synthesized single-coil data from the multi-coil raw data using the coil sensitivity maps (CSM) estimated by ESPIRiT [43]. We explored the reconstruction performance under two different sampling masks, each with two different acceleration factors. Specifically, pseudo-radial sampling [13] with 16 and 30 sampling lines and variable density random sampling (vds) with acceleration factors of 8 and 10, were adopted. The sampling lines in radial patterns are generated uniformly in the polar coordinate system at each time frame, while rotated by a small random angle across frames. The vds patterns undersample the grid by constructing a probability density function and randomly draw indices from that density to ensure undersampling less near the k-space origin and more in the periphery of k-space. In these single-coil cases, we trained our JotlasNet and the comparative networks from scratch for 50 epochs. In the multi-coil experiments, we also used the ESPIRiT [43] to estimate the CSMs for the network input, but we directly used the root sum of squares (RSS) images [44] as the ground truth for evaluation. The reason for this is that the estimated CSMs may not be accurate enough for the multi-coil data [1]. We employed the VISTA sampling mask [45] and evaluated the proposed JotlasNet under accelerations of 8, 12, and an ultra-high acceleration of 24. In VISTA-8, we trained the networks from scratch for 50 epochs, while finetuned them in other cases for 20 epochs using the trained weights in VISTA-8. The experiments in this dataset were conducted using one NVIDIA Quadro GV100 GPU with 32GB memory.

4.1.2. CMRxRecon Dataset

We used fully sampled raw data from 120 cases in CMRxRecon [46] for experiments. These data were acquired using a 3T Siemens MAGNETOM Vida scanner with a dedicated cardiac coil comprising 32 channels. Each case contains data from 6 to 12 slices, including short-axis, two-chamber, three-chamber, four-chamber, and long-axis views. We divided all the data cases into training, validation, and test sets at a ratio of 100:10:10. Consequently, we obtained 1247, 124, and 121 fully sampled training, validation, and test raw data samples/slices, respectively.

Only the multi-coil scenario was considered on the CMRxRecon dataset. We employed 1D pseudo-equispaced sampling masks [47, 48] (undersampling only in the phase-encoding direction). The central 24 columns were fully sampled as the auto-calibration signal region [43]. The accelerations of 8, 10, and 12 (without considering auto-calibration signals) were used. We also used the ESPIRiT to estimate the CSMs for the network input and directly utilized the RSS images as the ground truth for evaluation. In the 8X case, we trained the networks from scratch for 50 epochs. In other scenarios, we finetuned them for 20 epochs using the weights trained in the 8X case. The experiments in this dataset were conducted using one NVIDIA A100 GPU with 80GB memory.

4.1.3. Comparative Methods and Metrics

We compared our proposed JotlasNet with four state-of-the-art (SOTA) DUNs for dynamic MRI reconstruction, including LplusS-Net [34], ISTA-Net [17], DCCNN [16] and SLR-Net [15]. All comparative networks adopted the network architecture and parameter settings provided in their respective papers, and were implemented using their open-source code. The only difference lies in retraining them on the datasets we used. We also provided the zero-filled reconstruction results and the fully sampled ground truth as the baseline and label, respectively. We evaluated the reconstruction performance using the peak signal-to-noise ratio (PSNR) and structural similarity index measure (SSIM) as the metrics.

4.2. Single-coil Results

In Tab.2, we present the quantitative results of various networks on the OCMR dataset (single-coil). The symbol ‘-’ indicates that LplusS-Net cannot be trained on the corresponding sampling cases, which is due to the instability of SVD gradients [49] and the occurrence of NaN (not a number) values when computing specific matrix SVD in TensorFlow. From the quantitative metrics, it can be observed that JotlasNet achieves the highest PSNR and SSIM across all experiments under different sampling patterns. Additionally, we provide the corresponding inference times, demonstrating comparable reconstruction speeds achieved by our network. The slightly longer time is mainly attributed to the computation of SVD in the low-rank layers, since the computational complexity of SVD on an $n \times n$ matrix is $\mathcal{O}(n^3)$, whereas the computational complexity of convolutional layers is only $\mathcal{O}(n^2)$. However, the low-rank prior

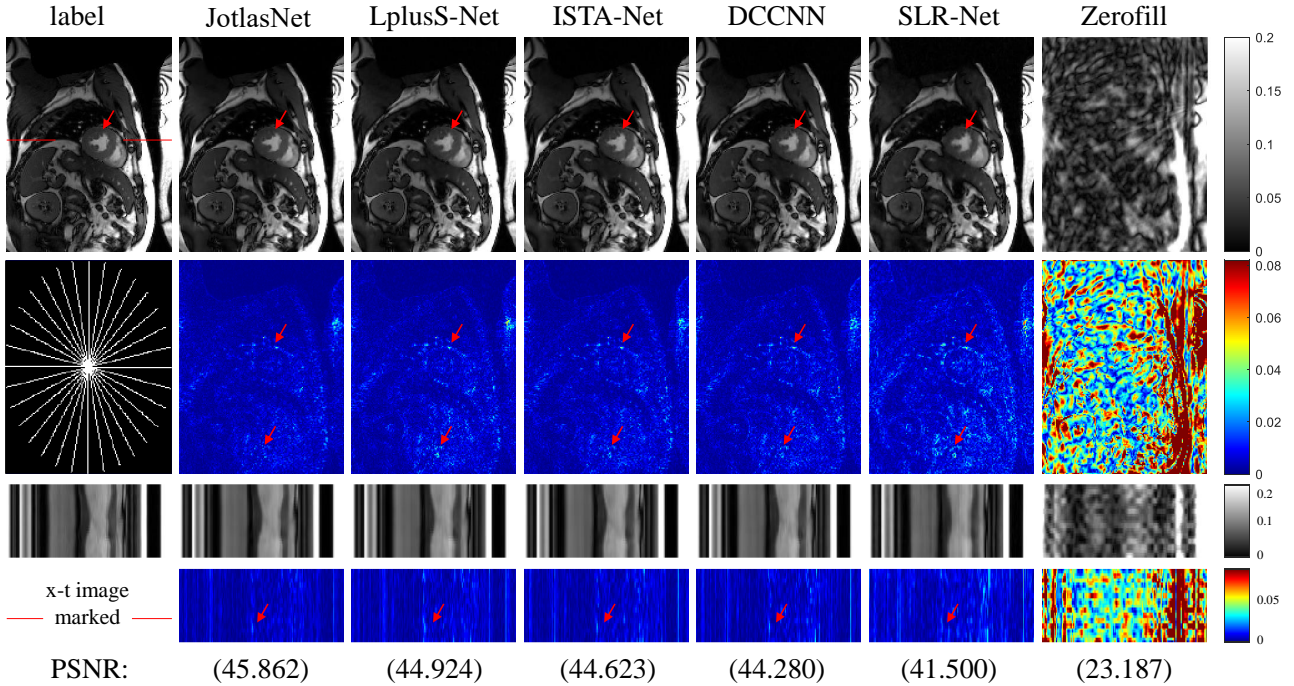


Figure 2: Reconstruction results on the OCMR dataset (single-coil) using radial sampling with 16 lines. The first row shows the reconstructed images at a specific time frame, and the second row shows the corresponding error maps, except for the first image depicted the sampling mask. The third and fourth rows show the x-t images and the corresponding error maps, respectively. The position of x-t images is marked with red lines on the label image. The PSNR values respected to this test image are also listed.

Table 2

Reconstruction Performance on OCMR Dataset (single-coil). The metrics are reported by the mean PSNR/SSIM on the test set. The inference time is in seconds.

	radial-16	radial-30	vds-8	vds-10	TIME
JotlasNet	41.708/0.982	43.231/0.987	41.671/0.981	34.979/0.949	0.92
L+S-Net	41.197/0.979	43.013/0.986	-	-	0.32
ISTA-Net	40.816/0.978	42.962/0.986	41.107/0.979	34.793/0.948	0.18
DCCNN	40.671/0.977	42.897/0.986	40.659/0.976	34.599/0.947	0.15
SLR-Net	38.635/0.964	40.212/0.971	39.056/0.968	33.880/0.934	0.36

enables the network to better utilize the redundancy in the data, thus facilitating improved image reconstruction [21]. Visualization results under radial-16 are shown in Fig.2. We display the reconstructed images of a particular data from the test set in the figure, along with the reconstruction results of a specific frame and x-t slice. It can be observed that our JotlasNet can reconstruct clearer textures while preserving details better. From the error maps, our network achieves better reconstruction performance in regions with more complex tissue and more intense motion.

4.3. Multi-coil Results

In Tables 3 and 4, we present the quantitative results of various methods on the OCMR and CMRxRecon datasets (multi-coil). From the quantitative metrics, it can be observed that our method achieves a significant improvement of over 1dB in PSNR compared to the second-best method. In Fig.3, we display the reconstruction results under 4X equispaced sampling patterns on the CMRxRecon dataset.

Table 3

Reconstruction Performance on OCMR Dataset (multi-coil). The metrics are reported by the mean PSNR/SSIM on the test set.

	VISTA-8	VISTA-12	VISTA-24
JotlasNet	37.508/0.971	36.262/0.957	34.030/0.948
L+S-Net	35.504/0.954	35.134/0.953	33.330/0.942
ISTA-Net	36.576/0.964	35.956/0.962	33.288/0.947
DCCNN	35.095/0.928	34.227/0.923	31.726/0.903
SLR-Net	34.212/0.953	32.151/0.936	28.512/0.891

Our JotlasNet can produce reconstructed images with lower errors while better preserving details. We highlight regions with noticeable differences in the error maps using red boxes in the visualized images. In the cardiac region, our network excels in restoring the shape and texture of the heart and preserving its edges. Additionally, even under ultra-high acceleration factors (e.g., 24-fold VISTA undersampling), our method effectively reconstructs images and outperforms SOTA methods.

We further compare our JotlasNet with CineVN model (MRM 2025) [31], which extends the end-to-end variation network [29] into spatiotemporal dynamic MRI. Another SOTA method, T2LR-Net (CIBM 2024) [21], is also compared. CineVN holds a total of 2.7M parameters (about 4 times more than JotlasNet), and is trained on the OCMR dataset with four NVIDIA A100 GPUs in parallel. Since the

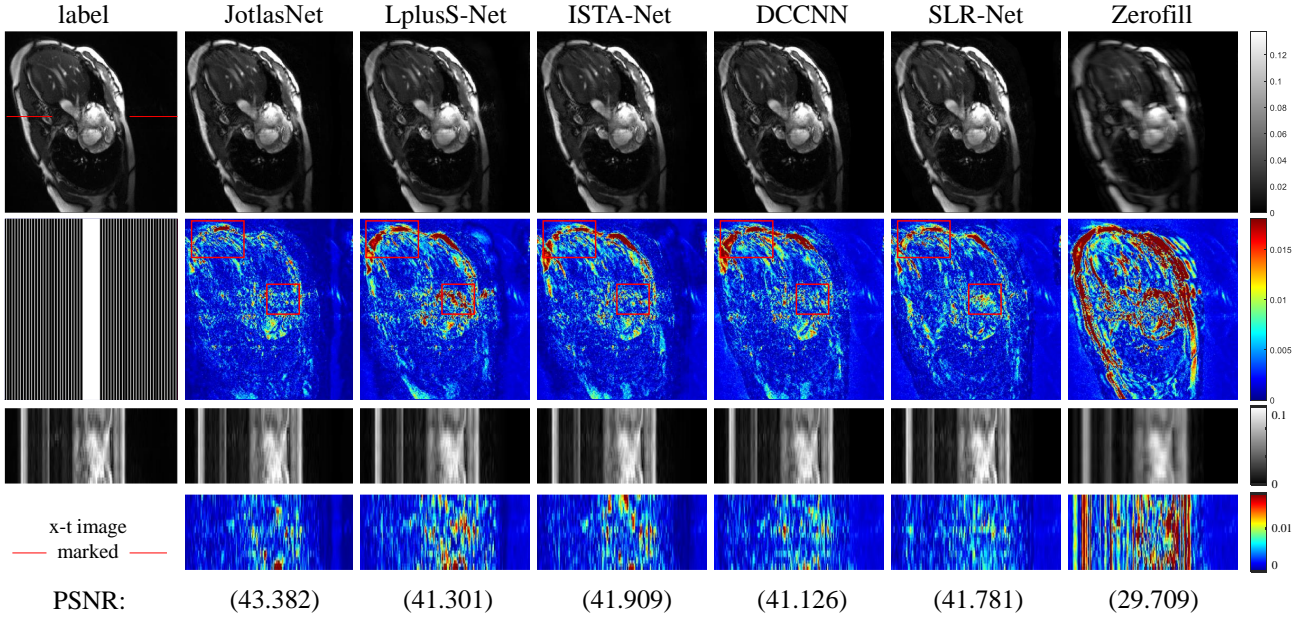


Figure 3: Reconstruction results on the CMRxRecon dataset (multi-coil) using 4X equispaced sampling. The first row shows the reconstructed images at a specific time frame, and the second row shows the corresponding error maps, except for the first image depicted the sampling mask. The third and fourth rows show the x-t images and the corresponding error maps, respectively. The position of x-t images is marked with red lines on the label image. The PSNR values respected to this test image are also listed.

Table 4

Reconstruction Performance on CMRxRecon Dataset (multi-coil). The metrics are reported by the mean PSNR/SSIM on the test set.

	4X	8X	10X
JotlasNet	38.228/0.961	35.631/0.951	34.960/0.948
L+S-Net	37.623/0.945	35.332/0.933	34.663/0.930
ISTA-Net	37.832/0.953	35.444/0.942	34.792/0.939
DCCNN	36.744/0.927	34.757/0.916	34.199/0.913
SLR-Net	37.464/0.942	34.709/0.926	34.019/0.922

Table 5

Reconstruction Performance of JotlasNet, CineVN, and T2LR-Net. The metrics are reported by mean \pm standard derivation.

	VISTA-8		VISTA-12	
	PSNR	SSIM	PSNR	SSIM
JotlasNet	40.791 \pm 3.733	0.981 \pm 0.014	40.047 \pm 3.161	0.973 \pm 0.014
CineVN (MRM 2025)	40.975 \pm 4.319	0.981 \pm 0.006	40.349 \pm 4.186	0.979 \pm 0.006
T2LR-Net (CIBM 2024)	40.404 \pm 4.602	0.978 \pm 0.012	39.856 \pm 4.299	0.963 \pm 0.018

data splitting is different with ours, We selected 10 data samples from the intersection of our test set and the CineVN test set for evaluation. The quantitative results are listed in Tab.5. The visualization results are shown in Fig.4. It is observed that our JotlasNet achieves comparable performance versus CineVN but with much fewer parameters and computation resources, which may attribute to the utilization of the tensor low-rank and sparse priors in JotlasNet while CineVN only employs the UNet to implicitly learn the spatiotemporal prior information.

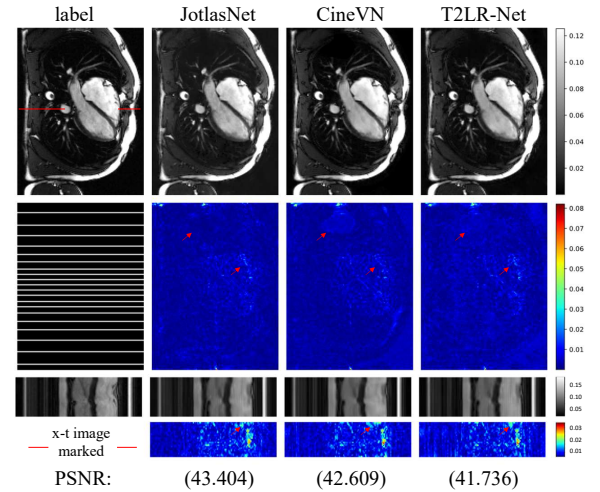


Figure 4: Reconstruction results of JotlasNet, CineVN, and T2LR-Net on the OCMR dataset (multi-coil) using 8-fold VISTA sampling.

4.4. Abalation Study

Under the radial-16 case, we conducted ablation experiments using OCMR single-coil data, as shown in Tab.6. Model-1 represents our JotlasNet; model-2 utilizes the algorithm proposed by SLR-Net, as described in (7), to solve our proposed tensor low-rank and sparse model and unfold it into a network. Model-3 is the network without the sparse prior. Model-4 and 5 represent networks without the low-rank prior, which are unfolded from the ISTA algorithm as (4). The distinction is that model-4 employs the AST operator

Table 6

Abalation study. The metrics are reported as mean \pm standard deviation.

model num	unrolled from	low rank	sparse	CNN constraint	PSNR	SSIM
1(ours)	Alg. 1	✓	AST	0	41.708 \pm 2.569	0.982 \pm 0.007
2	SLR-Net Alg.	✓	AST	0	41.629 \pm 2.576	0.981 \pm 0.007
3	ISTA	✓	×	0	40.788 \pm 2.520	0.978 \pm 0.008
4	ISTA	×	AST	0	41.617 \pm 2.582	0.981 \pm 0.008
5	ISTA	×	ST	0	41.428 \pm 2.592	0.980 \pm 0.008
6	ISTA	×	AST	0.001	41.588 \pm 2.618	0.981 \pm 0.008
7	ISTA	×	AST	0.01	40.950 \pm 2.528	0.977 \pm 0.008
8	ISTA	×	AST	0.1	36.997 \pm 2.253	0.947 \pm 0.014

proposed by us, while model-5 uses the traditional ST operator with only one threshold. From the comparison between model-1 and 2, it can be observed that the network unfolded by our proposed Alg.1 achieves better reconstruction results since Alg.1 exhibits a simple yet efficient structure similar to the single-prior ISTA. Comparing model-1 with 3 and 4, it can be seen that the dual-prior network achieves superior results compared to the single-prior network. From the comparison between model-4 and 5, it can be concluded that our proposed AST operator effectively enhances the network's ability to exploit sparsity, thereby achieving better reconstruction results.

As mentioned in Section 3.2, the CNNs learning the low-rank or sparse transformations are subjected to no constraints in our implementation. We use model-4 as the baseline to analyze the impact of CNN constraints on the network. Specifically, on top of the MSE loss in model-4, we incorporate the inverse constraint on the CNN-learned sparse transforms, akin to ISTA-Net [17] and SLR-Net [15],

$$\begin{aligned}
 Loss = & \sum_{(\mathcal{X}_{GT}, \mathbf{b}) \in \Omega} \|\mathcal{X}_{GT} - f_{net}(\mathbf{b}|\theta)\|_F^2 \\
 & + \zeta \sum_{n=1}^N \|\tilde{\mathcal{D}}_n \circ \mathcal{D}_n(\mathcal{X}_{n-1}) - \mathcal{X}_{n-1}\|_F^2, \quad (20)
 \end{aligned}$$

where ζ is the hyperparameter controlling the strength of the inverse constraint. We set ζ to 0.001, 0.01, and 0.1 to investigate the impact of the CNN constraint on the network. The results are shown in model-6 to 8. Compared with model-4 where $\zeta = 0$, it can be observed that the network's performance deteriorates as the CNN constraint strengthens. This indicates that inverse constraint forces CNNs to solely learn explicit sparse characteristics, without further integrating their implicit feature extraction capabilities.

Additionally, we also investigated the optimal number of iterations of JotlasNet under the radial-16 pattern in single coil scenario, as the results are shown in Fig.5. It can be observed that the PSNR increase slowly when the number of iterations exceeds 15. Therefore, in order to balance the reconstruction performance and computational efficiency, we set the number of iterations to 15 in our experiments.

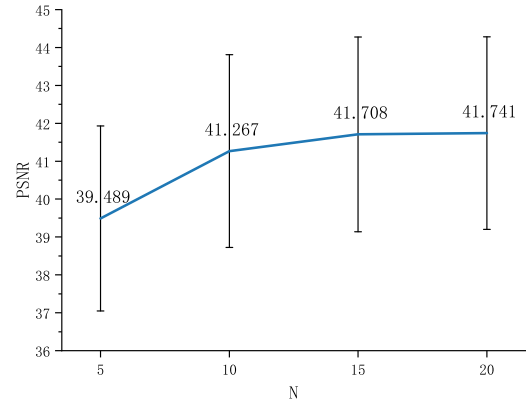


Figure 5: The PSNR of JotlasNet under different numbers of iterations (N). The blue line shows the mean PSNRs while the error bars represents the standard deviations.

5. Discussion

5.1. Interpretive Insight of LR and S layers

We show the intermediate results from different iterations of JotlasNet under radial-16 pattern in single coil scenario in Fig.6. In the early iterations (1-5), the LR layer focuses on the background while the S layer captures the edges, as indicated by the red arrows. In the middle iterations (6-10), the LR layer tends to smooth the textures due to its ability to capture correlation information, while the S layer adds the image details inside the smooth regions, as indicated by the red boxes. In the later iterations (11-15), the LR along with the S layer jointly remove the noise and refine the textures, as the PSNR increases slowly.

5.2. Rethinking the Structure of Neural Networks

We compare the composite splitting algorithm that incorporates joint low-rank and sparsity priors with the ISTA algorithm that utilizes low-rank plus sparse priors. We analyze the DUNs derived from these two algorithms to reconsider neural network architecture. The former has been elaborately described earlier, while the latter utilizes the following model and can be directly solved by ISTA [34]:

$$\min_{\mathcal{X}} \frac{1}{2} \|\mathbf{A}(\mathcal{L} + \mathcal{S}) - \mathbf{b}\|_2^2 + \lambda_1 \mathcal{R}(\mathcal{L}) + \lambda_2 \mathcal{S}(\mathcal{S}), \quad (21)$$

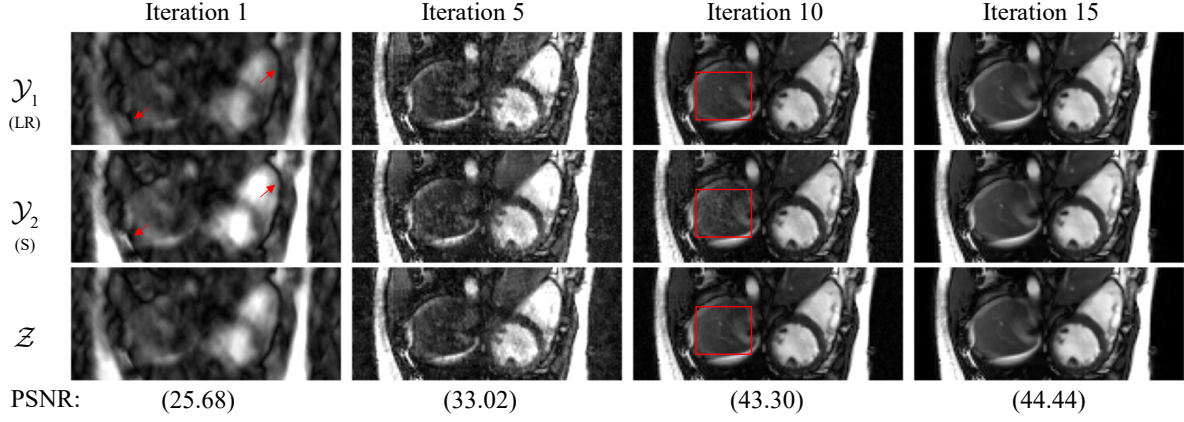


Figure 6: The intermediate results from different iterations of JotlasNet. The symbols are the same as Alg.1. The LR and S layers as well as their combination are shown along the vertical direction while the horizontal axis represents the different iterations. The corresponding PSNRs are also listed below the images.

$$\begin{cases} \bar{\mathcal{L}} &= \mathcal{L}^n - \mu \mathbf{A}^H [\mathbf{A}(\mathcal{L}^n + \mathcal{S}^n) - \mathbf{b}] \\ \bar{\mathcal{S}} &= \mathcal{S}^n - \mu \mathbf{A}^H [\mathbf{A}(\mathcal{L}^n + \mathcal{S}^n) - \mathbf{b}] \\ \mathcal{L}^{n+1} &= \text{prox}_{\mu\lambda_1 \mathbf{R}}(\bar{\mathcal{L}} - \mathcal{S}^n) \\ \mathcal{S}^{n+1} &= \text{prox}_{\mu\lambda_2 \mathbf{S}}(\bar{\mathcal{S}} - \mathcal{L}^{n+1}) \end{cases}, \quad (22)$$

The simplified diagrams of the networks unfolded from equations (16) and (22) are illustrated in Fig.7. Fig.7a depicts the structure of unfolding equation (16), representing the simplified diagram of our proposed network, while Fig.7b illustrates the structure of unrolling equation (22). The projection operations associated with low-rank and sparse constraints are represented by LR and S layers, respectively. Operations involving gradient descent and interactions between low-rank and sparse outputs are depicted by translucent squares, and interactions between iterations are represented by translucent lines. It is observed that for the network unfolded from equation (16), which exploits the joint utilization of low-rank and sparse priors, LR and S layers appear in a parallel configuration. Conversely, for the network unfolded from equation (22), which separates low-rank and sparse parts, LR and S layers appear in a serial configuration. This observation may provide partial interpretability to the structure of neural networks and offer insights for the design of DUNs.

5.3. Limitations and Future Work

Our proposed JotlasNet leverages jointly low-rank and sparse prior. Utilizing the low-rank prior often involves computing SVD. However, as mentioned in Section 4.2, the gradients of SVD exhibit numerical instability, particularly when two repeated singular values occur, leading to NaN gradients and hindering the training process [49]. Given the necessity for thousands of training steps, this risk is considerable. Hence, we plan to investigate gradient computation techniques for SVD and focus on developing differentiable SVD to address this issue in future work. Additionally, the computational complexity of SVD is high, which increases

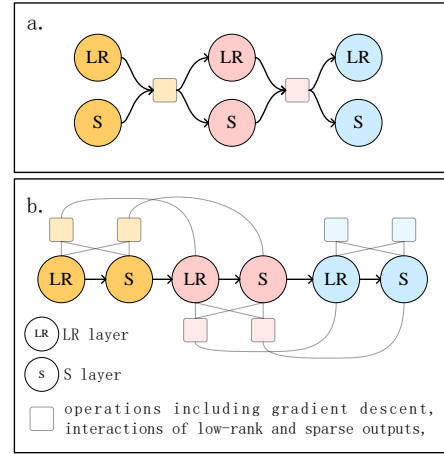


Figure 7: Simplified diagrams of the networks unfolded from equations (16) and (22). (a) The network unfolded from equation (16), representing the simplified diagram of our proposed network. (b) The network unfolded from equation (22).

the inference time of the network. Therefore, we will also explore methods for utilizing low-rank prior without relying on SVD [10] and integrate them into DUNs.

Furthermore, in this paper, we chose low-rank and sparse priors, two widely used and proven effective priors in past MRI reconstruction, to construct JotlasNet. In fact, within the framework of the composite splitting algorithm, we can replace LR and S layers with other priors, such as total variation prior [13], sparse prior in temporal Fourier domain [8], and other traditional priors. Moreover, we can integrate cutting-edge research in neural networks, such as introducing transformers to extract and utilize global feature priors, while using CNNs to extract local feature priors. These avenues will be the focus of our future research.

Additionally, many works have incorporated a coil sensitivity map estimation (SME) module to refine the CSMs at each iteration, which further improves the reconstruction

performance [29, 30], especially when autocalibration data is limited. We will explore the integration of the SME module into JotlasNet to enhance the reconstruction performance in the future work.

6. Conclusion

In this paper, we introduced a novel JotlasNet, representing the first attempt to jointly utilize transformed tensor low-rank and sparse priors. The low-rank and sparse domains are learned by CNNs. High-dimensional data correlations are exploited through the tensor nuclear norm. A novel AST operator was proposed to replace the conventional ST operator for sparse constraint. AST utilizes self-attention mechanism to learn individual thresholds for each channel, enhancing the flexibility of the network in utilizing sparse priors. Additionally, we designed an iterative algorithm based on the composite splitting algorithm to solve the model, further unrolling it into the proposed JotlasNet. The network exhibits a simple yet efficient parallel structure. Extensive experiments on the OCMR and CMRxRecon datasets demonstrated that our JotlasNet achieved superior reconstruction performance in both multi-coil and single-coil MRI reconstruction tasks. We posit that the framework we proposed carries profound implications for various models incorporating joint priors, extending beyond the interaction of low-rank and sparse priors and transcending the realm of dynamic MRI reconstruction applications.

Acknowledgments

This work is supported by the National Natural Science Foundation of China [grant number 62371167]; the Natural Science Foundation of Heilongjiang [grant number YQ2021F005].

References

- [1] M. J. Muckley, B. Riemenschneider, et al., Results of the 2020 fastMRI challenge for machine learning MR image reconstruction, *IEEE Trans Med Imaging* 40 (2021) 2306–2317.
- [2] M. Lustig, D. L. Donoho, J. M. Santos, J. M. Pauly, Compressed sensing MRI, *IEEE signal processing magazine* 25 (2008) 72–82.
- [3] M. Lustig, D. Donoho, J. M. Pauly, Sparse MRI: The application of compressed sensing for rapid MR imaging, *Magnetic Resonance in Medicine* 58 (2007) 1182–1195.
- [4] S. Boyd, N. Parikh, E. Chu, B. Peleato, J. Eckstein, et al., Distributed optimization and statistical learning via the alternating direction method of multipliers, *Foundations and Trends® in Machine learning* 3 (2011) 1–122.
- [5] M. V. Afonso, J. M. Bioucas-Dias, M. A. Figueiredo, Fast image recovery using variable splitting and constrained optimization, *IEEE Trans Image Processing* 19 (2010) 2345–2356.
- [6] A. Beck, M. Teboulle, A fast iterative shrinkage-thresholding algorithm for linear inverse problems, *SIAM journal on imaging sciences* 2 (2009) 183–202.
- [7] J. Huang, S. Zhang, D. Metaxas, Efficient MR image reconstruction for compressed MR imaging, *Medical Image Analysis* 15 (2011) 670–679.
- [8] H. Jung, K. Sung, K. S. Nayak, E. Y. Kim, J. C. Ye, k-t FOCUSS: a general compressed sensing framework for high resolution dynamic MRI, *Magnetic Resonance in Medicine* 61 (2009) 103–116.
- [9] S. Ravishanker, Y. Bresler, MR image reconstruction from highly undersampled k-space data by dictionary learning, *IEEE transactions on medical imaging* 30 (2010) 1028–1041.
- [10] Z.-P. Liang, Spatiotemporal imaging with partially separable functions, in: *2007 4th IEEE international symposium on biomedical imaging: from nano to macro*, IEEE, 2007, pp. 988–991.
- [11] J. He, Q. Liu, A. G. Christodoulou, C. Ma, F. Lam, Z.-P. Liang, Accelerated high-dimensional MR imaging with sparse sampling using low-rank tensors, *IEEE Trans Med Imaging* 35 (2016) 2119–2129.
- [12] R. Otazo, E. Candes, D. K. Sodickson, Low-rank plus sparse matrix decomposition for accelerated dynamic MRI with separation of background and dynamic components, *Magnetic resonance in medicine* 73 (2015) 1125–1136.
- [13] S. G. Lingala, Y. Hu, E. DiBella, M. Jacob, Accelerated dynamic MRI exploiting sparsity and low-rank structure: k-t SLR, *IEEE Trans Med Imaging* 30 (2011) 1042–1054.
- [14] K. Gregor, Y. LeCun, Learning fast approximations of sparse coding, in: *Proceedings of the 27th international conference on international conference on machine learning*, 2010, pp. 399–406.
- [15] Z. Ke, W. Huang, Z.-X. Cui, J. Cheng, S. Jia, H. Wang, X. Liu, H. Zheng, L. Ying, Y. Zhu, et al., Learned low-rank priors in dynamic MR imaging, *IEEE Trans Med Imaging* 40 (2021) 3698–3710.
- [16] J. Schlemper, J. Caballero, J. V. Hajnal, A. N. Price, D. Rueckert, A deep cascade of convolutional neural networks for dynamic MR image reconstruction, *IEEE Trans Med Imaging* 37 (2017) 491–503.
- [17] J. Zhang, B. Ghanem, ISTA-Net: Interpretable optimization-inspired deep network for image compressive sensing, in: *IEEE CVPR conference*, 2018, pp. 1828–1837.
- [18] D. L. Donoho, De-noising by soft-thresholding, *IEEE transactions on information theory* 41 (1995) 613–627.
- [19] C. Lu, J. Feng, Y. Chen, W. Liu, Z. Lin, S. Yan, Tensor robust principal component analysis with a new tensor nuclear norm, *IEEE transactions on pattern analysis and machine intelligence* 42 (2019) 925–938.
- [20] M. E. Kilmer, C. D. Martin, Factorization strategies for third-order tensors, *Linear Algebra and its Applications* 435 (2011) 641–658.
- [21] Y. Zhang, P. Li, Y. Hu, T²LR-Net: An unrolling network learning transformed tensor low-rank prior for dynamic MR image reconstruction, *Computers in Biology and Medicine* (2024) 108034.
- [22] Y. Zhang, X.-Y. Liu, B. Wu, A. Walid, Video synthesis via transform-based tensor neural network, in: *Proceedings of the 28th ACM International Conference on Multimedia*, 2020, pp. 2454–2462.
- [23] T. G. Kolda, B. W. Bader, Tensor decompositions and applications, *SIAM review* 51 (2009) 455–500.
- [24] J. Huang, S. Zhang, H. Li, D. Metaxas, Composite splitting algorithms for convex optimization, *Computer Vision and Image Understanding* 115 (2011) 1610–1622.
- [25] Y. Zhang, X. Li, W. Li, Y. Hu, Deep unrolling shrinkage network for dynamic MR imaging, in: *2023 IEEE International Conference on Image Processing (ICIP)*, 2023, pp. 1145–1149. doi:10.1109/ICIP49359.2023.10223077.
- [26] D. Liang, J. Cheng, Z. Ke, L. Ying, Deep magnetic resonance image reconstruction: Inverse problems meet neural networks, *IEEE Signal Processing Magazine* 37 (2020) 141–151.
- [27] V. Monga, Y. Li, Y. C. Eldar, Algorithm unrolling: Interpretable, efficient deep learning for signal and image processing, *IEEE Signal Processing Magazine* 38 (2021) 18–44.
- [28] H. K. Aggarwal, M. P. Mani, M. Jacob, MoDL: Model-based deep learning architecture for inverse problems, *IEEE Trans Med Imaging* 38 (2018) 394–405.
- [29] A. Sriram, J. Zbontar, T. Murrell, A. Defazio, C. L. Zitnick, N. Yakubova, F. Knoll, P. Johnson, End-to-end variational networks for accelerated MRI reconstruction, in: *Medical Image Computing and Computer Assisted Intervention—MICCAI 2020: 23rd International Conference, Lima, Peru, October 4–8, 2020, Proceedings, Part II* 23, Springer, 2020, pp. 64–73.

- [30] Z. Fabian, B. Tinaz, M. Soltanolkotabi, HUMUS-Net: Hybrid unrolled multi-scale network architecture for accelerated MRI reconstruction, *Advances in Neural Information Processing Systems* 35 (2022) 25306–25319.
- [31] M. Vornehm, J. Wetzl, D. Giese, F. Fürtrohr, J. Pang, K. Chow, R. Gebker, R. Ahmad, F. Knoll, Cinevn: Variational network reconstruction for rapid functional cardiac cine mri, *Magnetic Resonance in Medicine* 93 (2025) 138–150.
- [32] J. Xiang, Y. Dong, Y. Yang, FISTA-Net: Learning a fast iterative shrinkage thresholding network for inverse problems in imaging, *IEEE Transactions on Medical Imaging* 40 (2021) 1329–1339.
- [33] Y. Zhang, P. Li, Y. Hu, Dynamic MRI using learned transform-based tensor low-rank network (LT2LR-NET), in: *2023 IEEE 20th International Symposium on Biomedical Imaging*, 2023, pp. 1–4. doi:10.1109/ISBI53787.2023.10230437.
- [34] W. Huang, Z. Ke, Z.-X. Cui, J. Cheng, Z. Qiu, S. Jia, L. Ying, Y. Zhu, D. Liang, Deep low-rank plus sparse network for dynamic MR imaging, *Medical Image Analysis* 73 (2021) 102190.
- [35] X. Chen, W. Xia, Z. Yang, H. Chen, Y. Liu, J. Zhou, Z. Wang, Y. Chen, B. Wen, Y. Zhang, SOUL-Net: A sparse and low-rank unrolling network for spectral CT image reconstruction, *IEEE Transactions on Neural Networks and Learning Systems* (2023).
- [36] Y. Zhong, M. Huang, J. Li, Y. Wang, Z. Hu, Y. Li, D. Liang, H. Zheng, N. Zhang, JSLRNet: Joint sparse and low-rank unfolding network for MR image reconstruction, in: *Medical Imaging with Deep Learning*, 2024.
- [37] P. L. Combettes, J.-C. Pesquet, A proximal decomposition method for solving convex variational inverse problems, *Inverse problems* 24 (2008) 065014.
- [38] M. Zhao, S. Zhong, X. Fu, B. Tang, M. Pecht, Deep residual shrinkage networks for fault diagnosis, *IEEE Transactions on Industrial Informatics* 16 (2019) 4681–4690.
- [39] D. P. Kingma, J. Ba, Adam: A method for stochastic optimization, *arXiv preprint arXiv:1412.6980* (2014).
- [40] M. D. Zeiler, Adadelata: an adaptive learning rate method, *arXiv preprint arXiv:1212.5701* (2012).
- [41] M. Abadi, P. Barham, J. Chen, Z. Chen, A. Davis, J. Dean, M. Devin, S. Ghemawat, G. Irving, M. Isard, et al., TensorFlow: A system for Large-Scale machine learning, in: *12th USENIX symposium on operating systems design and implementation*, 2016, pp. 265–283.
- [42] C. Chen, Y. Liu, P. Schniter, M. Tong, K. Zareba, O. Simonetti, L. Potter, R. Ahmad, OCMR (v1. 0)—open-access multi-coil k-space dataset for cardiovascular magnetic resonance imaging, *arXiv preprint arXiv:2008.03410* (2020).
- [43] M. Uecker, P. Lai, M. J. Murphy, P. Virtue, M. Elad, J. M. Pauly, S. S. Vasanawala, M. Lustig, ESPIRiT—an eigenvalue approach to autocalibrating parallel MRI: where SENSE meets GRAPPA, *Magnetic resonance in medicine* 71 (2014) 990–1001.
- [44] P. B. Roemer, W. A. Edelstein, C. E. Hayes, S. P. Souza, O. M. Mueller, The NMR phased array, *Magnetic resonance in medicine* 16 (1990) 192–225.
- [45] R. Ahmad, H. Xue, S. Giri, Y. Ding, J. Craft, O. P. Simonetti, Variable density incoherent spatiotemporal acquisition (VISTA) for highly accelerated cardiac MRI, *Magnetic resonance in medicine* 74 (2015) 1266–1278.
- [46] C. Wang, J. Lyu, S. Wang, C. Qin, K. Guo, X. Zhang, X. Yu, Y. Li, F. Wang, J. Jin, et al., CMRxRecon: an open cardiac MRI dataset for the competition of accelerated image reconstruction, *arXiv preprint arXiv:2309.10836* (2023).
- [47] F. Knoll, T. Murrell, A. Sriram, N. Yakubova, J. Zbontar, M. Rabbat, A. Defazio, M. J. Muckley, D. K. Sodickson, C. L. Zitnick, et al., Advancing machine learning for MR image reconstruction with an open competition: Overview of the 2019 fastMRI challenge, *Magnetic resonance in medicine* 84 (2020) 3054–3070.
- [48] J. Zbontar, F. Knoll, A. Sriram, T. Murrell, Z. Huang, M. J. Muckley, A. Defazio, R. Stern, P. Johnson, M. Bruno, et al., fastMRI: An open dataset and benchmarks for accelerated MRI, *arXiv preprint arXiv:1811.08839* (2018).
- [49] W. Wang, Z. Dang, Y. Hu, P. Fua, M. Salzmann, Robust differentiable SVD, *IEEE Transactions on Pattern Analysis and Machine Intelligence* 44 (2021) 5472–5487.